

Separating Thermal and Nonthermal X-Rays in Supernova Remnants I: Total Fits to SN 1006 AD

K.K. Dyer, S.P. Reynolds, K.J. Borkowski

North Carolina State University, Physics Dept. Box 8202, Raleigh NC 27695-8202

G.E. Allen

MIT Center for Space Research NE80-6015, 70 Vassar St Cambridge, MA 02139

R. Petre

NASA's GSFC, LHEA Code 666, Greenbelt MD 20771

Kristy_Dyer@ncsu.edu

ABSTRACT

The remnant of SN 1006 has an X-ray spectrum dominated by nonthermal emission, and pre-ASCA observations were well described by a synchrotron calculation with electron energies limited by escape. We describe the results of a much more stringent test: fitting spatially integrated *ASCA* GIS (0.6 – 8 keV) and *RXTE* PCA (3 – 10 keV) data with a combination of the synchrotron model *sresc* newly ported to XSPEC and a new thermal shock model *vpshock*. The new model can describe the continuum emission above 2 keV well, in both spatial distribution and spectrum. We find that the emission is dominantly nonthermal, with a small but noticeable thermal component: Mg and Si are clearly visible in the integrated spectrum. The synchrotron component rolls off smoothly from the extrapolated radio spectrum, with a characteristic rolloff frequency of 3.1×10^{17} Hz, at which the spectrum has dropped about a factor of 6 below a powerlaw extrapolation from the radio spectrum. Comparison of TeV observations with new TeV model images and spectra based on the X-ray model fits gives a mean post-shock magnetic field strength of about $9 \mu G$, implying (for a compression ratio of 4) an upstream magnetic field of $3 \mu G$, and fixing the current energy content in relativistic electrons at about 7×10^{48} erg, resulting in a current electron-acceleration efficiency of about 5%. This total energy is about 100 times the energy in the magnetic field. The X-ray fit also implies that electrons escape ahead of the shock above an energy of about 30 TeV. This escape could result from an absence of scattering magnetohydrodynamic waves above a wavelength of about 10^{17} cm. Our results indicate that joint thermal and nonthermal fitting, using sophisticated models, will be required for analysis of most supernova-remnant X-ray data in the future.

1. Introduction

Since supernova shocks are one of the few mechanisms known to be capable of providing adequate energy to supply the pool of Galactic cosmic rays, supernova remnants (SNRs) have long been suspected as the primary site of Galactic cosmic ray acceleration, at least up to the slight steepening in the cosmic-ray spectrum at a few 10^{15} eV, known as the “knee.” Direct evidence for energetic particles comes from radio observations of synchrotron emission from 1–10 GeV electrons. However, in the cosmic rays observed at Earth, at a few GeV electrons are about 50 times less numerous than cosmic-ray ions, whose spectrum is an unbroken power law from 10^9 eV to 10^{15} eV. These considerations raise two questions: 1) Do SNRs accelerate ions? 2) Are they capable of accelerating *any* particles to energies of 10^{15} eV? This paper addresses the second question by demonstrating the presence of electrons of energies of hundreds of TeV in the remnant of SN 1006 AD.

High-energy electrons can produce X-rays via nonthermal bremsstrahlung and synchrotron radiation, and gamma-rays from inverse-Compton upscattering of any photons present. Relativistic protons can produce γ -rays from the decay of π^0 particles produced in inelastic collisions with background gas. These processes have recently been studied in detail by Sturmer et al. (1997), Gaisser, Protheroe, & Stanev (1998) and Baring et al. (1999). The analysis of X-ray and gamma-ray observations of shell supernova remnants may give direct evidence bearing on both questions above. In this paper we will interpret observed X-rays and TeV gamma-rays as primarily synchrotron radiation and inverse-Compton upscattered cosmic microwave background radiation, respectively, and will obtain maximum electron energies and electron shock acceleration efficiencies – crucial information for understanding shock acceleration in general, and the origin of Galactic cosmic rays.

The earliest evidence of nonthermal X-ray emission in a shell supernova remnant came from the featureless spectrum of SN 1006 AD (G327.6–1.4) (Becker et al. 1980), explained as the loss-steepened extrapolation of the radio synchrotron spectrum by Reynolds & Chevalier (1981). However, early data were poor and the models were simplistic. Thermal models by Hamilton, Sarazin, & Szymkowiak (1986) seemed able to produce a featureless X-ray spectrum, given a high degree of elemental stratification in ejecta. However, observations by *ASCA* (Koyama et al. 1995) showed unmistakable evidence for nonthermal emission in the rims, along with thermal, line-dominated emission in the interior. Reynolds (1996) demonstrated that detailed, self-consistent synchrotron models could be constructed which adequately described the pre-*ASCA* integrated spectrum of SN 1006 as the diminishing extension of the radio spectrum, reproducing the slope reported by Koyama et al. (1995) in the rim. While Laming (1998) proposed a modified thermal bremsstrahlung model based on the model of Hamilton et al. (1986), even the author concluded that it is not an appropriate fit for SN 1006.

Since then, several more shell SNRs have been shown to have nonthermal, non-plerionic emission. In addition to SN 1006 (Koyama et al. 1995), G347.3-0.5 (RJ J1713.7-3946) (Koyama et al. 1997; Muraishi et al. 2000; Slane et al. 1999) has nearly featureless X-ray spectra clearly domi-

nated by nonthermal emission. Some remnants, while not dominated by nonthermal emission in the *ASCA* band, show other evidence pointing to its presence. *OSSE* observations of Cassiopeia A at 400-1250 keV (The et al. 1996) are well described by a broken power law, steepening to higher energies (Allen et al. 1997a). RCW 86 (Vink, Kaastra & Bleeker 1997) shows anomalously low abundances when fit with thermal models. When the fit includes a synchrotron model the abundances fall within expected ranges (Borkowski et al. 1999).

An important consequence of synchrotron X-ray emission was pointed out by Pohl (1996) and Mastichiadis & de Jager (1996). Electrons capable of producing keV synchrotron photons in magnetic fields of a few microgauss will also produce high-energy photons by inverse-Compton scattering any photon fields. In particular, inverse-Compton upscattering of cosmic-microwave-background photons can produce TeV gamma rays, and Pohl (1996) explicitly predicted a range for the expected TeV flux of SN 1006 (subsequently found by the CANGAROO air Čerenkov telescope). The predicted flux depends only on the electron distribution, so it can be used, in conjunction with observed synchrotron fluxes, to deduce a mean magnetic-field strength in a remnant. Subsequent extensive calculations by Sturmer et al. (1997), Gaisser et al. (1998), and Baring et al. (1999) included this effect.

However, nonthermal X-ray emission from shell supernova remnants could be due to bremsstrahlung from nonrelativistic electrons with energies of a few tens of keV (Asvarov et al. 1990) rather than synchrotron radiation from electrons with energies of hundreds of TeV. Careful models (e.g., Baring et al. 1999 as well as Reynolds 1996) show that in neither case are straight power-laws to be expected. Synchrotron spectra should all be steepening (convex up) while bremsstrahlung spectra, resulting from the lowest energy cosmic ray electrons departing from the Maxwellian tail, ought to be flattening (concave up). Allen et al. (1997a) showed that the *ASCA* spectrum from SN 1006 steepens to higher energies, and the discovery of the predicted TeV gamma rays by the CANGAROO collaboration (Tanimori et al. 1998) provided strong evidence that the nonthermal X-ray emission in SN 1006 is in fact synchrotron radiation. However, nonthermal bremsstrahlung is expected to be important for some remnants, and as more observations become available above 10 keV, it will be necessary to discriminate between synchrotron and nonthermal bremsstrahlung. (While most analyses, e.g., Mastichiadis & de Jager (1996), conclude that the TeV emission from SN 1006 is inverse-Compton, Aharonian & Atoyan (1999) and Berezhko, Ksenofontov, & Petukhov (1999) assert that the π^0 -decay mechanism may be partly responsible.)

Despite the strong evidence for curvature, a straight power law is still commonly regarded as a defining characteristic of X-ray synchrotron radiation in shell supernova remnants, as it is in Crab-like supernova remnants and active galactic nuclei. While power laws will certainly be a better description of synchrotron emission produced by the particle spectra expected in SNR shock acceleration than quasi-thermal exponential continua, all SNR X-ray synchrotron continua are expected to be substantially curved, even over a relatively narrow energy range. However, in almost all published studies, nonthermal SNR X-ray emission has been described by a power law. This purely phenomenological treatment, while characterizing the emission, fails to explain

its origin. Power laws cannot continue forever rising as the frequency drops, a fact camouflaged by the rapidly dropping response of X-ray instruments at low energies. Broken power laws can avoid this “infrared catastrophe,” but they still duck the question of the origin of the emission and its relation to the lower-energy synchrotron spectrum. Since no Galactic supernova remnant has X-ray emission bright enough to lie on the unbroken extrapolation of the radio spectrum (Reynolds & Keohane 1999), extrapolating from radio measurements will grossly over-predict the X-ray flux, as demonstrated in Figure 1. The spectrum must drop significantly below the observed power law in the radio to be consistent with the X-ray flux measurements. A good physical model must both fit this turnover and explain the mechanism causing the spectral curvature.

Some spectral modeling of SNR synchrotron X-rays has been done using other descriptions. While a power law represents a spectrum with no curvature, the maximum curvature likely to result from shock acceleration comes from an electron spectrum with an exponential cutoff. In the approximation in which each electron radiates all its energy at the peak frequency of the single-particle synchrotron emissivity (the “ δ -function approximation”), this implies a photon spectrum $S(E) \propto \exp((E/E_m)^{-1/2})$. Aharonian & Atoyan (1999) modeled synchrotron emission from SN 1006 using this expression, with a constant maximum energy E_m . As was demonstrated in Reynolds (1998) the δ -function approximation is not accurate well above the turnover energy. In addition, the electron distribution will vary throughout the remnant. A convolution of the electron synchrotron emissivity with the calculated electron distribution at each location in the remnant is required. The model described in this paper includes the full electron emissivity.

It is important to understand and accurately characterize the synchrotron emission in SNRs. If the emission mechanism in those SNRs with clear nonthermal continua is synchrotron radiation, then many SNRs could have varying amounts of synchrotron X-ray emission, contributing part of the continuum emission alongside the thermal lines and continuum. As demonstrated by RCW 86 (Borkoswki et al. 2000a), such an unmodeled component stymies thermal fits by preventing accurate measurements of shock temperatures and elemental abundances. Understanding either the thermal or nonthermal X-ray emission from SNRs requires appropriate modeling of both components. This paper applies a model that assumes Sedov dynamics and a power-law distribution of electrons up to a maximum energy E_{max} , which can vary with time and with location in the remnant. In general, the maximum energy attained by electrons in the shock acceleration process could be limited by one of several factors — electrons above this energy could escape from the remnant, the remnant could be so young it has not had time to accelerate particles beyond some E_{max} , or E_{max} could be the energy at which radiative losses balance further acceleration. Normally, a remnant’s spectrum would first be limited by age, and then by radiative losses, unless escape prevented either of the other limits from being reached.

In this paper we analyze new *RXTE* observations, along with archival *ASCA* observations, in Section 2. We discuss the escape model, *sresc*, in Section 3, along with our new gamma-ray modeling, and compare *sresc* to thermal models and a thermal+power law model in Section 4. In Section 5, we discuss the elemental abundances we infer from the joint thermal-nonthermal model,

and compare them to predictions by Nomoto, Thielemann, & Yokoi (1984) and Iwamoto et al. (1999) and discuss the implications of our results for the efficiency of electron acceleration. We summarize our conclusions in Section 6.

2. Observations

2.1. RXTE

On 18–19 February 1996, SN 1006 was observed for 21 kiloseconds with the Proportional Counter Array (PCA) of the *RXTE* satellite. A summary of *RXTE* observations can be found in Table 1. The PCA is a spectrophotometer comprised of an array of five co-aligned proportional counter units that are mechanically collimated to have a field-of-view of 1° at full width, half maximum. The array is sensitive to 2–60 keV photons and has a maximum collecting area of about 7000 cm^2 (Jahoda et al. 1996). The instrument was pointed at a location on the bright north-eastern rim ($\alpha_{2000} = 15^{\text{h}} 4^{\text{m}} 0$, $\delta_{2000} = -41^\circ 48'$). The angular diameter of SN 1006 is small enough (about $30'$) that the entire remnant was in the field-of-view of the instrument. The total event-detection rate during this observation is $26.43 \pm 0.06 \text{ count s}^{-1}$ in the range 3–10 keV. The background spectrum of the PCA data was estimated using version 1.5 of the program *pcabackest*. This version includes estimates of the charged-particle and diffuse cosmic X-ray backgrounds based on the “VLE” count rate during observations of “blank-sky” regions and an estimate of the background associated with the decay of radioactive material that is activated when the spacecraft passes through the South Atlantic Anomaly. The count rate of the estimated background is $15.46 \pm 0.06 \text{ count s}^{-1}$ (3–10 keV). Time intervals during which (1) one or more of the five proportional counter units is off, (2) SN 1006 $< 10^\circ$ above the limb of the Earth, (3) the background model is not well defined, and (4) the nominal pointing direction of the detectors $> 0^\circ 02'$ from the specified pointing direction are excluded from the present analysis. The count-rate attributed to SN 1006 during the 6.6 kiloseconds of the observation that satisfies these four criteria is $11.0 \pm 0.1 \text{ count s}^{-1}$.

During the proposal phase we were concerned with possible contamination from Lupus and special effort was made to obtain off-source spectra in addition to spectra from SN 1006 AD. Lupus, a thermal source, is not expected to produce significant emission above 3 keV and preliminary examination of *RXTE* data from Lupus reveal spectra very similar to the cosmic X-ray background. This data has also been analyzed by Allen (Allen et al. 1997a, Allen et al. 2000, in preparation).

2.2. ASCA

SN 1006 has been observed several times with *ASCA* in the performance verification phase and later cycles. A summary of the *ASCA* observations used in this paper can be found in Table 2. Backgrounds for SIS were obtained from off-source portions of the same chip. Backgrounds for

GIS were taken from the 3 November 1999 dark earth event files. Since SN 1006 is located in the galactic anticenter, 15° off the plane, galactic emission should not contribute significantly to the background.

In Section 4.1 we fit observations of the north limb of SN 1006, using areas from a single SIS chip plus the equivalent portions of the GIS. In Section 4.2 we fit three ASCA observations of the whole remnant (GIS 2 & 3, for a total of six data sets) obtained from 1993-1996. Since RXTE has no spatial resolution and a 1° field of view only the full fields of the ASCA GIS can be simultaneously fit with RXTE observations.

3. The Escape Model

Two models were proposed for the pre-ASCA integrated spectrum of SN 1006 in Reynolds (1996), with different mechanisms causing the rolloff in the electron spectrum: an age-limited model, which required an upstream magnetic field of only $0.6 \mu\text{Gauss}$, and an escape-limited model, in which the upstream magnetic field could be much larger. The TeV detection (Tanimori et al. 1998) constrains the mean magnetic field in the remnant, as described below, to be of order $10 \mu\text{Gauss}$, ruling out the age-limited model. (The third category of model, radiative-loss-limited, could not fit the pre-ASCA data.) We therefore consider only the escape-limited model as a description for SN 1006.

3.1. Assumptions in the model

The model *sresc* presented in this paper and discussed in Reynolds (1998) describes SNR emission with electron energies limited by escape, which accounts correctly for variation of shock-acceleration efficiency with obliquity and for post-shock radiative and adiabatic losses. The model makes the following assumptions: 1) the remnant dynamics are well described by the Sedov self-similarity solution (we eliminate the singularity at the center of the Sedov solution by truncating the emissivity at a radius where the velocity of the shock= $10,000 \text{ km s}^{-1}$, an ejection velocity appropriate to Type Ia supernovae); 2) the remnant is expanding into a uniform medium with a uniform magnetic field, B_1 ; 3) the density increases by a fixed factor r downstream of the shock – this means that the magnetic field strength increases by a factor between 1 and r as the tangential component is compressed, depending on the angle between the shock normal and the upstream magnetic field; 4) the postshock magnetic field evolves by flux-freezing, with no turbulent amplification after the initial compression; 5) the relativistic electrons have short postshock diffusion lengths so that their density evolves in the same way as the thermal-gas density. Electrons that escape are allowed to diffuse upstream from the shock along magnetic field lines, producing a faint “halo”.

Recent models of nonlinear shock acceleration (e.g., Berezhko Yelshin & Ksenofontov Berezhko

et al. 1999; Baring et al. 1999, Ellison, Berezhko, & Baring 2000) predict that high efficiencies of particle acceleration mimic a lossy shock, with overall compression ratios considerably higher than 4, and correspondingly lower thermal-gas temperatures. Since both the escape model and the thermal models we use below predict only post-shock quantities, they are largely independent of the compression ratio, which is used only to infer pre-shock values of density and magnetic-field strength based on the post-shock inferences. The thermal inferences have strictly no dependence on the compression ratio, while the details of the fainter nonthermal emission in the escape model (where the magnetic field is parallel to the shock normal) are slightly dependent on r . However, for the values of $r \sim 7$ given by the nonlinear model of Berezhko et al. (1999), the predictions are indistinguishable from $r = 4$. In any case, the reader should bear in mind that all statements about pre-shock quantities assume some value of the compression ratio.

The model describes the drop-off in synchrotron emission compared to a straight power-law. As adapted for XSPEC (the X-Ray Spectral Fitting Package, Arnaud 1996) it can be applied to remnants with different total radio flux densities and spectral indices. Predicted images depend on the time at which the remnant was assumed to enter the Sedov stage, and at the aspect angle between the upstream magnetic field and the line of sight, but these parameters do not affect the integrated spectrum. In fact, the escape model can be applied to any remnant which has been interacting with uniform-density material with a uniform magnetic field for most of its lifetime, as long as the electron spectrum is in fact cut off by escape, and not by finite remnant age or by radiative losses. This can only be checked by reference to the expressions for those maximum energies, as given for instance in Reynolds (1998); we require $E_{\max}(\text{escape}) < \min(E_{\max}(\text{age}), E_{\max}(\text{loss}))$. The assumption of Sedov dynamics, rather than (say) a late stage of self-similar driven wave into uniform material, makes little difference to the total spectrum. Since most of the X-ray emission is produced closely behind the shock, the detailed form of the drop-off of synchrotron emissivity is not critical. (It would be important in modeling radio images, but not for the integrated spectrum.)

The window for applicability of the escape model is probably intermediate in a remnant's life, between early times when the age limitation is most restrictive (and in which a core-collapse remnant may be interacting with stellar-wind material with a circumferential magnetic field), and late times when radiative losses may be most influential.

There are several reasons why electrons above some E_{\max} could escape the remnant. While an intuitively obvious limit for an electron's gyroradius is the SNR diameter, it has been shown that other mechanisms dominate before this limit is reached (Lagage & Cesarsky 1983). In our diffusive acceleration picture, acceleration occurs as electrons scatter resonantly from magnetohydrodynamic waves in the upstream and downstream fluids. While the downstream medium is likely to be highly turbulent, supporting waves of all wavelengths, this may not be true of the upstream medium, where waves are probably produced by the accelerated particles themselves. Without reference to a detailed mechanism, in the escape model we assume that magnetohydrodynamic scattering waves are much weaker above some wavelength λ_{\max} which corresponds to an energy E_{\max} of electrons at this gyroradius. Since electrons with gyroradius r_g scatter resonantly with waves of wavelengths

$\lambda = 2\pi r_g = 2\pi(E/eB)$, electrons will escape upstream once their energy reaches an E_{max} given by

$$E_{max} = \lambda_{max} e B_1 / 4 \quad (1)$$

(after averaging over pitch angles) where B_1 is the upstream magnetic field strength. Unlike the age and loss-limited cases (Reynolds 1998), here E_{max} does not change with time or depend on the angle between the shock normal and upstream magnetic field. This energy then corresponds to a photon frequency

$$\nu_{max} = 1.05 \times 10^{15} \lambda_{17}^2 B_{\mu G}^3 \left(\frac{r}{4}\right) \quad (2)$$

where $\lambda_{17} \equiv \lambda_{max}/10^{17}$ cm, $B_{\mu G}$ is the upstream magnetic field measured in microgauss and r is the compression ratio. Only one power of r is involved since E_{max} depends on B_1 , and B_2 only enters because ν_{max} reflects the particles with $E = E_{max}$ radiating in the stronger post-shock magnetic field.

The shape of the cutoff could depend on the detailed distribution of waves, but is likely to be no steeper than an exponential. The escape model assumes an electron distribution given by $N(E) = K E^{-p} \exp(-E/E_{max})$ at the shock, and evolves it appropriately in the remnant interior, including radiative (synchrotron and inverse-Compton) and adiabatic expansion losses. At each point a synchrotron volume emissivity is found by convolving the single-electron emissivity with this distribution. Model images (shown in Figure 8b) are formed by integrating along a raster scan of lines of sight and the spectrum is found by integrating the flux over the image at each frequency. The models are discussed in more detail in Reynolds (1998).

3.2. The model *sresc*

The escape-limited model is particularly well suited to algorithmic fitting processes like those in XSPEC, since the departure from a power-law is described by a single parameter; a universal function describes the shape of the rolloff, and the one parameter simply locates the rolloff in frequency. Note from Equation 2 that fixing $\nu_{rolloff}$ does not fix λ_{max} , B_1 , or r , but only the combination $\lambda_{max}^2 B_1^3 r$. The model can be found in XSPEC 11 under the name *sresc*. The models are also expected to be available with the next release of CIAO, the Chandra software.

The model has three parameters:

1. the radio flux measurement (*norm*) at 1 GHz
2. α , the radio spectral index (flux density $\propto \nu^{-\alpha}$)
3. the characteristic rolloff frequency (Hz), called *rolloff* (for *sresc*, $\nu_{rolloff} = 5.3\nu_{max}$, for historical reasons; $\nu_{rolloff}$ is the frequency at which the spectrum has dropped by a factor of ~ 6 below the extrapolated radio power law; Reynolds 1998)

The spectral index and 1 GHz flux for SNRs are fixed by radio observations. For Galactic SNRs, they can be found at Green’s website¹.

Finally it should be emphasized that *sresc* is only designed to model Sedov-phase remnants whose maximum electron energy is limited by electron escape. It also presumes a remnant in or close to the Sedov dynamical phase, which has been encountering a uniform upstream medium with a constant magnetic field. It is not appropriate for remnants in a highly inhomogeneous environment. It should not be applied to core-collapse remnants still interacting with stellar-wind material (although it could be appropriate for some core-collapse remnants which have expanded beyond the pre-supernova medium). In addition, if the compression ratio r is very much greater than 4, the model will overestimate fluxes from the “poles” where the emission is faintest, though the integrated spectrum will not be strongly affected.

Since *srcut* (synchrotron radiation cut-off model, Reynolds & Keohane 1999) describes the simplest possible synchrotron source with a minimum of assumptions, it can be applied to remnants of unknown provenance or dynamical stage more safely. Until an appropriate range of models, including different dynamical stages and different external media, is available, *srcut* represent a significant improvement over fitting a power law especially if the purpose of the fit is to account for the nonthermal emission so that a thermal model may be accurately fit. Models appropriate for core-collapse remnants, and describing age- and loss-limited cases have been calculated (Reynolds 1997; Reynolds & Keohane 1999), and will also be made available in XSPEC when practicable.

3.3. Uncertainties in radio flux and spectral index

Since the *sresc* model has only one free parameter (*rolloff*) with both the spectral index (α) and the 1 GHz flux (*norm*) specified by radio measurements, errors in these values will have an effect on the synchrotron fits, and therefore on values in the co-fitted thermal model. The sensitivity to α is substantial, since a variation of 0.05, over a frequency range between 10^9 Hz and 10^{18} Hz (4 keV), results in an offset of a factor of 3.

In addition, since many interferometer radio maps may miss smoothly distributed radio flux, care must be taken if the flux in spatially distinct regions is to be used as input to the model. In Section 4.1 we used *sresc* to fit part of the remnant. To obtain the appropriate value of *norm* from our 1.34 GHz interferometer map (Reynolds & Gilmore 1986), which is missing a good deal of flux, we added a uniform flux across the image to raise the total flux in the remnant to the prediction from the radio single dish measurement of 15.9 Jy, using a spectral index $\alpha= 0.6$ to scale the 1 GHz total flux of 19 Jy (Green 1998). We measured the flux in the subregion, then scaled the flux

¹Green D.A., 1998, ‘A Catalogue of Galactic Supernova Remnants (1998 September version)’, Mullard Radio Astronomy Observatory, Cambridge, United Kingdom (available on the World-Wide-Web at <http://www.mrao.cam.ac.uk/surveys/snrs/>”).

to the 1 GHz value for input into the *sresc* model using $S_{\nu_1}/S_{\nu_2} = (\nu_1/\nu_2)^{-\alpha}$.

3.4. TeV gamma-ray consequences of *sresc*

In the *sresc* model, the spatial dependence of the electron distribution is entirely fixed by the assumption of Sedov dynamics and the assumption that the relativistic-electron density tracks the thermal-gas density, with the specification of E_{\max} and B_1 . This dependence is calculated taking into account synchrotron and cosmic microwave background inverse-Compton losses as well as adiabatic expansion losses. Adding a radio flux density and spectral index fixes the normalization of the distribution, given the value of B_1 . Given the electron distribution everywhere, it is a simple matter to calculate the morphology and spectrum of TeV gamma-ray emission. To extract this prediction, we have added the inverse-Compton kernel described in Baring et al. (1999), basically the full Klein-Nishina result, to *sresc*. Here it is natural to work in photon energies instead of frequencies. The Klein-Nishina cross-section is given by

$$\sigma_{\text{K-N}}(\varepsilon_s, \gamma_e; \varepsilon_\gamma) = \frac{2\pi r_0^2}{\varepsilon_s \gamma_e^2} \left[2q \log_e q + 1 + q - 2q^2 + \frac{\Gamma^2 q^2 (1-q)}{2(1+\Gamma q)} \right], \quad (3)$$

with $\Gamma = 4\varepsilon_s \gamma_e$ being the parameter that governs the importance (when $\Gamma \gtrsim 1$) of photon recoil and Klein-Nishina effects, and with

$$q = \frac{\varepsilon_\gamma}{4\varepsilon_s \gamma_e (\gamma_e - \varepsilon_\gamma)}, \quad 0 \leq q \leq 1, \quad (4)$$

where $\varepsilon_s m_e c^2$ is the initial photon energy, $\varepsilon_\gamma m_e c^2$ is the upscattered (final) photon energy, and $\gamma_e = (E_e + m_e c^2)/m_e c^2$. The constant $r_0 = e^2/(m_e c^2)$ is the classical electron radius. This result assumes isotropic soft photon fields, the case for the cosmic microwave background radiation.

The inverse Compton emissivity for isotropic photon fields is then (e.g., Blumenthal & Gould 1970)

$$\frac{dn_\gamma(\varepsilon_\gamma)}{dt} = c \int N_e(\gamma_e) d\gamma_e \int d\varepsilon_s n_\gamma(\varepsilon_s) \sigma_{\text{K-N}}(\varepsilon_s, \gamma_e; \varepsilon_\gamma), \quad (5)$$

where $n_\gamma(\varepsilon_s)$ is the distribution of seed photons, and $N_e(\gamma_e)$ is the calculated electron energy distribution at each point in the remnant (Reynolds 1998). This expression is used with the blackbody photon distribution (expressed in terms of photon energies)

$$n_\gamma(\varepsilon_s) = n_{\text{BB}}(\varepsilon_s) \equiv \frac{\varepsilon_s^2}{\pi^2 \lambda_c^3} \frac{1}{e^{\varepsilon_s/\Theta} - 1}, \quad \Theta = \frac{kT}{m_e c^2}, \quad (6)$$

with $T = 2.73$ K so that $\Theta = 4.6 \times 10^{-10}$. Here $\lambda_c = \hbar/(m_e c)$ is the Compton wavelength.

As with synchrotron emission, the inverse-Compton emissivity is calculated at each point in the remnant, and integrated along a raster scan of lines of sight to produce a gamma-ray image. Images at different photon energies are integrated over to produce a total spectrum.

4. Results

Since preliminary fits to the X-ray data were unable to constrain the absorbing column density, we turned to past observations. While Koyama et al. (1995) found an absorption of $1.8 \times 10^{21} \text{ cm}^{-2}$ most other observations point to lower absorption. The Schweizer-Middleditch star seen through SN 1006 has a color excess $E(B-V)$ of 0.12 (Blair, Long & Raymond 1996). From this, the empirical relation between color excess and column density (Gorenstein 1975) yields $N_H = 7.7 \times 10^{20} \text{ cm}^{-2}$. This is not in gross disagreement with previous *ROSAT* observations by Willingale et al. (1996), who found a column density of $(3.9 - 5.7) \times 10^{20} \text{ cm}^{-2}$. BeppoSAX observations by Vink et al. (2000) found an absorption of $(8.8 \pm 0.5) \times 10^{20}$. For fitting purposes we adopt a column density of $5 \times 10^{20} \text{ cm}^{-2}$ for all models. Details on the datasets used for fitting are summarized in Table 3. To account for instrumental differences and differences in background subtractions we allowed multiplicative offsets between all the data sets. The ratio of *RXTE* PCA to *ASCA* GIS data is given in Table 4, row 3. It varied between 0.63 and 0.70.

In the cases where a thermal and nonthermal model were fit, where the nonthermal model dominated the flux, the thermal model had little leverage to determine some parameters accurately. In particular, determining the absolute abundances (relative to hydrogen) requires fixing the level of thermal continuum, which is particularly difficult in the presence of synchrotron continuum emission. We believe the obvious line features can be analyzed with somewhat more confidence. Formal fits to the data resulted in overall high abundances, with correspondingly large errors, but we believe the ratios between abundances (in particular to silicon, whose $K\alpha$ emission is relatively well determined) are more reliable than the absolute values obtained, and give the ratios in Table 4. For the *sresc + vps shock* fit in Section 4.2.4 we reversed the process. Rather than fixing hydrogen and helium, we fixed silicon, the most obvious line present in the data, allowing the emission measure and other lines to adjust. This produced abundance ratios very close to fits with hydrogen and helium fixed but allowed us to obtain more reliable error ranges, including upper limits on hydrogen and helium.

SN 1006 presents a complicated mix of thermal and nonthermal spectra. It has been known from some time that emission from the rim of SN 1006 is almost entirely nonthermal (Koyama et al. 1995). Since the results of jointly fitting two models are rarely unique we constrained fits to the full remnant by first fitting the north rim with a nonthermal model, either power-law or *sresc*². We then used the parameters from the limb data to constrain the nonthermal model used on the entire remnant.

²Since *sresc* was designed to describe the spectrum from the remnant as a whole this is an approximation, though a reasonable one since the limbs dominate the total spectrum. In a future paper we will use spatially resolved versions of *sresc* to describe subsections of the SNR.

4.1. Model Fits to the North Limb

We selected *ASCA* SIS spectra obtained in the northeast observation (13 August 1993) from the single chips (SIS 0 chip 1, SIS 1 chip 3), with corresponding regions from GIS 2 and GIS 3. We fit these featureless spectra with a power law, as shown in Figure 3a. We obtained a photon index of 2.46 and a *norm* (photons keV⁻¹ cm⁻² s⁻¹ at 1 keV) of 8.09×10^{-3} , yielding a $\chi^2_\nu = 0.91$. All four datasets were allowed to vary by a constant – the ratios were SIS 0:1.00 SIS 1:0.91 GIS 2:1.01 GIS 3:0.76. Using the energy range, column density, and line centroids from Koyama et al. (1995) we were able to replicate their results to within 1σ . We obtained $\Gamma = 2.50^{+0.34}_{-0.63}$ (1σ), in agreement with $\alpha = 1.95 \pm 0.2$. (For power-law emission, using the explicit positive convention for α , the energy spectral index, $S_\nu \propto \nu^{-\alpha}$, and these quantities are related by $\alpha + 1 = \Gamma$, where Γ is the photon index.)

We then fit the same four data sets with *sresc*, as shown in Figure 3b. We froze the spectral index α at 0.60 and froze *norm* to the proportionate flux (as discussed in §3.3) of 2.54 Jy. This left one free parameter, *rolloff* = $3.06^{+0.1}_{-0.3} \times 10^{17}$ Hz yielding $\chi^2_\nu = 1.04$. The ratios between the datasets were SIS 0:1.00 SIS 1:1.02 GIS 2:1.14 GIS 3:0.88.

4.2. Model Fits to Full Remnant

Table 4 contains the results of the fits to the whole remnant, for each of several thermal models as described below. Included are the χ^2 and the number of degrees of freedom (DOF, row 1), the reduced χ^2 (row 2), the multiplicative offset used between the *RXTE* PCA and the *ASCA* GIS (row 3), the temperature found by each thermal model in units of keV (row 4) and the ionization timescale $\tau \equiv n_e t$ in units of s cm⁻³ (row 5). The fitted abundances are listed in rows 6-11, given as $\frac{\langle X/H \rangle}{\langle X/H \rangle_\odot}$ (by number, not mass, from Grevesse & Anders 1989), relative to silicon. Elements not listed could not be constrained by the data and were left at solar. In row 13 the amount (*norm*) of thermal/nonthermal component is given. For the powerlaw the normalization is photons keV⁻¹ cm⁻² s⁻¹ at 1 keV; for *sresc* the normalization is the 1 GHz radio flux. In row 14 the 0.6 – 10.0 keV flux of the thermal and nonthermal model is given. Finally, in row 15, the constraining nonthermal parameter is listed (power-law index for the power law, and ν_{rolloff} for *sresc*). This parameter is not allowed to vary, but is taken from the corresponding fit in Section 4.1. Each model was fit to the full dataset (six GIS datasets + *RXTE*) but is shown in the figures only with a single GIS and the *RXTE* dataset for clarity. All errors given are 1σ errors.

4.2.1. Nonequilibrium Ionization Model

The *ASCA-RXTE* observations of SN 1006 were first fit with *NEI*, a constant temperature non-equilibrium ionization model that describes an impulsively heated uniform and homogeneous gas

(Borkowski, Lyerly & Reynolds 2000b), released with XSPEC v11. The *nei* model, with elemental abundances held fixed at solar, produced a $\chi^2_{\nu}=3.27$ (see Figure 4). While the *nei* model represents the simplest non-equilibrium ionization description of a thermal shock, we do not expect it to be a good description since the physical case it describes is only appropriate in limited cases where all emitting material was shocked at the same time – such as individual clumps of gas rapidly overrun by the shock.

4.2.2. Plane Shock Model

The *vpshock* model is a plane-parallel shock model with varying abundances (Borkowski et al. 2000b, released with XSPEC 11) including nonequilibrium-ionization effects. It represents an improvement over the *nei* model by allowing a linear distribution of ionization timescale $\tau \equiv n_e t$ vs. emission measure between user-specified τ_{lower} and τ_{upper} . Normally one will set τ_{lower} equal to zero, for an ongoing shock, and we have done so. The abundances of O, Ne, Mg, Si, S, and Fe were allowed to vary. We fit the *ASCA* GIS + *RXTE* PCA data with *vpshock*, shown in Figure 5. Were this the only information we had on SN 1006 we would conclude that this is an acceptable description of the data. However, the absence of spectral lines in the limb data (fit in Section 4.1), indicates that a purely thermal explanation is not in fact adequate.

4.2.3. Power Law + Plane Shock Model

It was impossible to find a unique separation between the power-law and *vpshock* components based only on the full-remnant spectrum. Lower fluxes of the power-law component were compensated for by the thermal model with lower temperatures and higher abundances, with no outstanding fit. Instead, we allowed the limb data (§4.1) to fix the power-law photon index. With that photon index we set the highest possible *norm* that did not disagree with the *RXTE* PCA data. We then froze the power law parameters and fit a *vpshock* model, allowing the abundances to vary. The fit is shown in Figure 6.

4.2.4. Escape Limited Synchrotron + Plane Shock Model

We then fit an *sresc* model plus *vpshock*. We took the parameters for *sresc* from the limb fits (§4.1): $\alpha=0.60$, $\text{rolloff}=3.06 \times 10^{17}$ Hz, and *norm* (the 1 GHz flux)= 19 Jy. This left no free parameters in the *sresc* portion of the fit. We then added a *vpshock* component and allowed the elemental abundances to vary. The fit is shown in Figure 7 and the results are listed in Table 4. In the best fit *sresc* + *vpshock* model we found that 60% of the flux was synchrotron emission and the thermal emission comprised the 40% remaining X-ray flux. While the χ^2 for *sresc* + *vpshock* is identical to that of the power-law + *vpshock* fit, there is only one *sresc* + *vpshock* model, while

as discussed above, many power-law + *vshock* models were possible.

As discussed in Section 4, we fixed silicon, the line with the most information in the spectrum, and fit all other parameters. The results are shown in the Table 4, excepting hydrogen $0.00^{2.0E-3}$ and helium $0.00^{3.0E-3}$, for which it was only possible to find upper limits.

The parameters of *sresc* also yields spatial predictions. In Figure 8a we show the 1993 August 19 GIS 2 data selected from 2-10 keV, the portion of the spectrum where, according to *sresc* models, the SNR is completely dominated by nonthermal emission. In Figure 8b we show the predicted image of the model at 2 keV generated from the radio spectral index, the 1 GHz radio flux and the *sresc* parameter, *rolloff*. Both images have been convolved to $2'$. These images are strikingly similar, supporting the use of the synchrotron model.

4.3. Gamma-ray Observations of North Limb

Making use of the results of the above fits, we can also fit the TeV gamma-ray observations of SN 1006 by Tanimori et al. (1998). The fitted values for *sresc* with *vshock* produce a one-parameter family of predicted TeV gamma-ray spectra, since two parameters (basically magnetic-field energy density and relativistic-electron energy density, or K and B_1) are required to set the synchrotron normalization, and *norm* only fixes the product $KB^{1+\alpha}$. The value of ν_{rolloff} from the *sresc* fits fixes the product $\lambda_{\text{max}}^2 B_1^3$. Different choices of B_1 , then, imply different inferred values of λ_{max} , otherwise unobservable, and different values of the normalization constant K in the electron distribution. However, each value of K gives a different normalization to the inverse-Compton spectrum which has no dependence on magnetic field.

The integrated fluxes of $(4.6 \pm 2.0) \times 10^{-12}$ photons $\text{cm}^{-2} \text{s}^{-1}$ ($E \geq 1.7 \pm 0.5$ TeV) and $(2.4 \pm 1.2) \times 10^{-12}$ photons $\text{cm}^{-2} \text{s}^{-1}$ ($E \geq 3.0 \pm 0.9$ TeV) imply an energy spectral index of 2.15. Using this value, the fluxes imply monochromatic flux densities of 3.5×10^{-38} erg $\text{cm}^{-2} \text{s}^{-1} \text{Hz}^{-1}$ at $\nu = 4.1 \times 10^{26}$ Hz, and 1.0×10^{-38} erg $\text{cm}^{-2} \text{s}^{-1} \text{Hz}^{-1}$ at $\nu = 7.2 \times 10^{26}$ Hz. These fluxes are plotted in Figure 11, which also shows two gamma-ray spectra, for $B_1 = 3$ and $5 \mu\text{gauss}$ (and $r = 4$), constrained to have the same value of *norm*, i.e., varying in K . The observed TeV gamma-ray flux then fixes the magnetic field, along with K and λ_{max} . A value of $B_1 = 3 \mu\text{gauss}$ describes the data well, and implies $\lambda_{\text{max}} = 1.4 \times 10^{17}$ cm and $K = 5.9 \times 10^{-12}$ erg $^{p-1}$ cm^{-3} . Figure 12 shows the predicted image of gamma-ray emission at an energy of 1 TeV. If $r > 4$, all values of B_1 are multiplied by $4/r$.

5. Discussion

5.1. Thermal and nonthermal continuum

As expected, the simple non-equilibrium ionization model, *nei*, with solar abundances is a poor description to SN 1006. *vpshock* is a better fit but knowing that parts of the remnant are dominated by nonthermal emission we know that temperature and abundances change with the addition of a nonthermal model.

The power-law model was very difficult to constrain in conjunction with thermal models. *vpshock*, and we suspect other thermal models as well, can seemingly adapt to nearly any amount of power-law : larger amounts of power-law cause lower temperatures, as *vpshock* contributes less of the continuum, and higher abundances, as *vpshock* tries to account for line emission from a lower thermal continuum.

The *sresc* + *vpshock* described the *ASCA* and *RXTE* observations very well, at least as well as the best *vpshock* + power-law . In addition, if ν_{rolloff} is constrained from fits to the nonthermal dominated limb observation, then remarkably *sresc* has no free parameters – it uniquely specifies the synchrotron emission in the SNR. This result confirms that nonthermal X-ray emission can be well described by simple synchrotron model, and the synchrotron escape model, which has previously only been tested on integrated fluxes, provides a good description of the data.

High abundances of heavy elements in the *sresc* + *vpshock* model imply that thermal emission is strongly dominated by supernova ejecta, which became obvious only after a proper separation of nonthermal and thermal components. Elemental abundances in SN 1006 ejecta are clearly of great interest, but spatially-integrated GIS and *RXTE* spectra used in this work allow only for the most basic interpretation of thermal spectra.

The *vpshock* model is the best first approximation for modeling X-ray spectra from shocks dominated by heavy element ejecta. Because this model provides statistically and physically reasonable fits to spatially integrated GIS spectra, we briefly interpret our results. However, these are just preliminary results, a more detailed analysis of spatially-resolved spectra should provide more secure answers. In this future analysis, one needs to consider both the reverse and forward shock, instead of just one plane shock considered here. This analysis should also be based on full hydrodynamical models with the realistic Type Ia ejecta structure (Dwarkadas & Chevalier 1998).

By freezing silicon, we found the best fit model required no hydrogen or helium with a $1\text{-}\sigma$ upper limit of $\frac{\langle H \rangle}{\langle Si \rangle} = 2 \times 10^{-3}$ and $\frac{\langle He \rangle}{\langle Si \rangle} = 3 \times 10^{-3}$. We can use this to try and set an upper limit on the preshock density. From an upper limit on hydrogen of $\frac{\langle H \rangle}{\langle Si \rangle} = 2 \times 10^{-3}$ we obtain an upper limit on the preshock density of $0.014(4/r) \text{ cm}^{-3}$. This is somewhat less than n_H of 0.05–0.1 cm^{-1} (assuming $r = 4$) estimated by Dwarkadas & Chevalier (1998) in their detailed analysis of SN 1006. However, our value is poorly constrained, since it depends on determining the level of thermal continuum, which we cannot do with certainty in the presence of much stronger nonthermal

continuum.

But most emission in the *vpshock* model comes from heavy elements, presumably ejecta shocked by the reverse shock, and the temperature T and ionization timescale τ in the last column of Table 4 most likely refer to the reverse shock. We can roughly estimate the time-averaged electron density $\langle n_e \rangle$ in the shocked heavy-element plasma by assuming that most X-ray emission comes from material shocked in the last 500 yr (approximately half of the remnant’s age), which gives $\langle n_e \rangle \sim \tau/500 \text{ yr} = 0.24 \text{ cm}^{-3}$. This order of magnitude estimate, together with abundances and normalization of the *vpshock* model from Table 4, allows us to arrive at the total mass of X-ray emitting ejecta of $0.71 M_\odot$, a lot of it ($0.45 M_\odot$) in Fe. While the absolute numbers are uncertain, a high Fe mass is consistent with the Type Ia SN progenitor.

5.2. Elemental Abundances

Extensive theoretical work has been carried out by Iwamoto et al. (1999) and Nomoto et al. (1984) predicting abundances expected from different supernova types. However it has proved quite difficult in practice to compare theory directly to measured abundances in a SNR.

In Figure 9 we compare the measured abundances (Iwamoto et al. 1999) with a thermal model alone (*vpshock*), to abundances measured with a thermal + synchrotron model (*vpshock* + *sresc*). The abundances are given relative to Si. The predicted abundance of Si for the W7 model is $0.16 M_\odot$ and $0.12 M_\odot$ for the Type II model (Iwamoto et al. 1999). The abundances in our fits change significantly with the addition of the nonthermal model, bringing the measured abundances closer to models predicted by Nomoto et al. (1984). We can take this farther and compare abundances to those predicted for Type Ia and core-collapse SNRs. As shown in Figure 10, the *vpshock* + *sresc* model fit to the observations seems to agree better with Type Ia models, as expected for SN 1006; however, the uncertainties are large and the Type II model cannot be ruled out.

By fixing silicon and fitting all other parameters, we are also able to calculate the total mass in each element, which we give in Table 5. Most notably, with the *sresc* model we have found half a solar mass of iron, closer to theoretical predictions, possibly a first for Type Ia SNR. As demonstrated in the table, while our calculated masses are not in perfect agreement with the Type Ia models in Iwamoto et al. (1999), they are closer to the Type Ia models than the Type II models.

We believe these results represent an improvement in technique over past work, while at the same time considering the values obtained preliminary. Improved results can be obtained by analyzing spatially resolved regions where the thermal emission dominates (such as will be done in Paper II). In addition we have used only the simplest possible thermal model (an single non-equilibrium ionization model not being physically plausible). However from these preliminary results we can state confidently that accurate accounting for a possible nonthermal component will be a necessary precondition to using nucleosynthesis model predictions to interpret abundances in SNRs.

5.3. *sresc* inferences and cosmic-ray acceleration

5.3.1. Simple estimates

Even before the reported detection of SN 1006 in TeV gamma-rays by the *CANGAROO* collaboration (Tanimori et al. 1998), Pohl (1996) calculated expected TeV fluxes due to upscattering of cosmic microwave background photons by electrons of 10-100 TeV, and the subsequent detection has been widely accepted as direct evidence for the presence in SN 1006 of such electrons. Pohl calculated a range of values of predicted flux based on a homogeneous emitting volume; the results depended on the then poorly known electron spectrum.

Since the maximum photon energy ε_γ that can be produced by an electron of Lorentz factor γ_e upscattering photons of energy ε_s is given by $\varepsilon_{\gamma_e} = 4\gamma_e^2\varepsilon_s$, turning cosmic microwave background photons ($T = 2.73$ K $\Rightarrow \epsilon_0 = 2.4 \times 10^{-4}$ eV) into 4 TeV gamma-rays requires $\gamma \geq 6.5 \times 10^7$. Then the Klein-Nishina parameter $\Gamma \equiv 4\gamma_e\varepsilon_s = 0.1$ and the Thomson limit ($\Gamma < 1$) is marginally acceptable, at least for energies not too far above the *CANGAROO* thresholds. In that case, the inverse-Compton volume emissivity for a thermal distribution of seed photons scattered by an electron distribution $N_e(\gamma_e) = C\gamma_e^{-p}$ can be written (Rybicki & Lightman 1979, switching to photon frequencies for comparison with synchrotron)

$$j_\nu = \frac{h}{4\pi} \frac{dn_\gamma}{dt} = \frac{C(2\pi r_0^2)}{h^2 c^2} (kT)^{(p+5)/2} F(p) (h\nu)^{-(p-1)/2} \text{ erg cm}^{-3} \text{ s}^{-1} \text{ Hz}^{-1} \text{ sr}^{-1} \quad (7)$$

where $F(p) = 5.67(6.11)$ for $p = 2.1$ (2.2) (values appropriate for SN 1006). Rewriting the electron distribution as $N(E) = KE^{-p}$ with $K = C(m_e c^2)^{p-1}$, and taking $p = 2.2$, we can express the ratio of the synchrotron to inverse-Compton volume emissivities as

$$\frac{j_\nu(\text{SR})}{j_\nu(\text{IC})} = \frac{3.48 \times 10^{-12} K B_G^{1.6} \nu^{-0.6}}{2.35 \times 10^{-25} K \nu^{-0.6}} = 3.72 \times 10^3 B_{\mu G}^{1.6} \quad (8)$$

where $B_{\mu G}$ is the magnetic field in the radiating region in units of μG .

We can use this result to estimate the mean magnetic field in SN 1006, making the simplest assumptions of a homogeneous source coextensive in synchrotron and inverse-Compton emission. (The inverse-Compton emitting volume will always be at least as large as the synchrotron volume, larger if electrons diffuse to where the magnetic field is weak or negligible.) If no turnover has begun by the lower of the two *CANGAROO* energies, the ratio of the extrapolation of the synchrotron flux to the TeV flux at 1.7 TeV is about 1.4×10^5 , using a radio spectral index $\alpha = (p-1)/2 = 0.6$. This gives a mean magnetic field strength of $9.6 \mu G$.

The observed radio flux density at 1 GHz of 19 Jy (Green 1998) then requires $K = 2.8 \times 10^{-12} \text{ erg}^{p-1} \text{ cm}^{-3}$. Now the immediate post-shock relativistic electron density is given by

$$u_e \equiv \int_{E_l}^{E_h} EN(E) dE = \frac{K}{p-2} E_l^{2-p} \left(1 - \left(\frac{E_h}{E_l} \right)^{2-p} \right) \cong 5K E_l^{-0.2} \quad (9)$$

where E_h and E_l are the ends of the electron distribution, and we have assumed $E_h \gg E_l$. If we let $E_l = 0.5$ MeV, appropriate since a constant power-law in momentum will flatten in energy below mc^2 , we find a post-shock energy density

$$u_e = 2.3 \times 10^{-10} \text{ erg cm}^{-3} \quad (10)$$

which can be compared with the post-shock pressure

$$P_2 = \frac{3}{4} \rho_1 u_{\text{sh}}^2 = 9 \times 10^{-9} \left(\frac{u_{\text{sh}}}{3200 \text{ km s}^{-1}} \right)^2 \quad (11)$$

for a strong shock in a gas with adiabatic index 5/3. So this simple estimate implies a relativistic-electron acceleration efficiency in the shock of about 2.6%. Extension of the same momentum power-law to nonrelativistic energies would give a comparable amount of energy in nonrelativistic suprathermal electrons. If the shock is dominated by relativistic particles, the compression ratio could be as high as 7, dropping the post-shock pressure by about 50% and increasing the inferred efficiency by that factor.

If supernova remnants are to produce the Galactic cosmic rays, efficiencies of ion acceleration must be of order several tens of percent, so given that we do not know the ratio of electron to ion acceleration efficiency, these estimates seem reasonable. They also imply a total magnetic energy content in SN 1006 of

$$U_B \equiv \frac{4\pi R_{\text{sh}}^3}{3} \phi \frac{B^2}{8\pi} = 5.3 \times 10^{46} \text{ erg} \quad (12)$$

where ϕ is a volume filling factor of the emission, taken to be 1/4. This is far below equipartition, since the total relativistic-electron energy is

$$U_e = 3.3 \times 10^{48} \text{ erg} \quad (13)$$

assuming the same filling factor, and we have not taken account of ions. However, if the pre-shock magnetic field is of order $3 \mu\text{G}$, the post-shock field due to shock compression only will be about $10 \mu\text{G}$, so reaching equipartition would require major turbulent magnetic field amplification.

5.3.2. Model calculations

Using the full spectral code, we have calculated the spectrum shown in Figure 11, using the rolloff frequency value obtained from our best fit result above. Now fitting *sresc* produces only the value of

$$\nu_{\text{rolloff}} \equiv 5.3 \nu_{\text{max}} = 5.3 (1.82 \times 10^{18} E_{\text{max}}^2 B_2), \quad (14)$$

where B_2 is the post-shock magnetic-field strength and E_{max} is given by (1). (The factor 5.3 was introduced in converting the original models into XSPEC-readable format.) So

$$\nu_{\text{rolloff}} = 5.57 \times 10^{15} \left(\frac{\lambda_{\text{max}}}{10^{17} \text{ cm}} \right)^2 B_{\mu\text{G}}^3 \left(\frac{r}{4} \right). \quad (15)$$

There is no theoretical expectation for λ_{\max} , so any value of B_1 can produce a particular value of ν_{rolloff} . This degeneracy is then broken by the inverse-Compton predictions which do depend on B_1 .

In Figure 11, we show the model with our fitted value of $\nu_{\text{rolloff}} = 3.1 \times 10^{17}$ Hz, and $B_1 = 3 \mu\text{G} \Rightarrow \lambda = 1.4 \times 10^{17} (4/r)^{-1/2}$ cm. This model is able to reproduce the *CANGAROO* fluxes reasonably well. In the *sresc* model, the magnetic field behind the shock is compressed only, by a factor of between 1 and r depending on the shock obliquity, and drops with distance behind the shock. The mean value of B_2 is approximately $9 \mu\text{G}$, consistent with the simple estimate above. The required value of K is $5.9 \times 10^{-12} \text{ erg}^{p-1} \text{ cm}^{-3}$, about twice the simple estimate, implying

$$u_e = 4.8 \times 10^{-10} \text{ erg cm}^{-3} \Rightarrow U_e = 7.0 \times 10^{48} \text{ erg} \quad (16)$$

and a relativistic-electron acceleration efficiency $u_e/(3/4)\rho_1 u_{\text{sh}}^2 = 5.3\%$ – somewhat higher than the simple estimate. This value was not obtained, as was the simple estimate, by assuming the Thomson limit. Again, a somewhat higher compression ratio does not alter the electron energy density, but by dropping the post-shock pressure slightly, can increase this value by of order 50%.

The values of λ_{\max} and B_1 give $E_{\max} = 50$ ergs or 32 TeV from Equation (1); this energy is in the range of the upper limits to maximum energies of synchrotron X-rays allowable in twelve other Galactic remnants whose X-rays are dominantly thermal (and far below the “knee” at around 1000 TeV). The significance of this particular value of λ_{\max} , above which the level of magnetohydrodynamic turbulence is presumed to be much less, is not obvious; this is the first example of this form of determination of structure in the magnetic-fluctuation power spectrum.

Figure 12b shows the predicted image in gamma rays at 1 TeV. The modeling of the propagation of electrons escaping upstream is not constrained at all by X-ray fitting, since those electrons radiate in the weaker upstream magnetic field and hence contribute only a small amount of synchrotron flux. However, they contribute more significantly to the inverse-Compton flux. Imaging observations may allow improvements in the description of these escaping electrons. The width of the emission behind the shock is greater than for synchrotron X-rays, since the magnetic field also drops behind the shock. However, in our nonthermal models for SN 1006, a contact discontinuity separating shocked ISM from SN ejecta is still present (modeled by the cutoff radius at which material was shocked at 10^4 km s^{-1}), and the shock-accelerated electrons are not assumed to diffuse into that region.

There is no obvious reason that the NE limb, but not the SW, should be detected in TeV gamma rays, especially since both limbs have very similar X-ray spectra (Allen et al. 1997b). Tanimori et al. (1998) report that the upper limit on emission from the SW limb is about one-quarter of the emission detected from the NE. This result demands a lower relativistic-electron density by that factor. An unfortunate coincidence could allow the magnetic-field strength to be larger in the SW in such a way as to produce an identical synchrotron spectrum with a lower density of relativistic electrons. The magnetic field would need to be larger by at least $4^{2/(p+1)} = 2.4$. Other possible explanations are at least as contrived, such as greater line-of-sight component of the magnetic field in the SW compensating for a lower electron density. We are unable to offer any convincing physical

explanation at this time for the detection of only the northeast limb. We plan to search for spatial variations, such as variations in the value of ν_{rolloff} , between the limbs, which might help account for the lack of TeV emission from the SW, in our spatially resolved study.

6. Conclusions

1. The escape-limited synchrotron model, *sresc*, provides a good fit to integrated spectral observations of SN 1006 by *RXTE* and *ASCA* – the highest quality data to date. In addition, the spatial prediction closely matches the X-ray image in the energy range where the model applies.
2. The *sresc* model provides a significant improvement over the power-law models:
 - (a) *sresc* provides a more accurate description of the emission based on physical principles.
 - (b) *sresc* allows a clearer separation of thermal and nonthermal emission, constrained by radio observations
3. We believe an adequate description of the synchrotron emission leads to more accurate temperature and abundance measurements in the remaining thermal model, though better thermal inferences require both spatially resolved spectra (and models) and codes appropriate for ejecta dominated by heavy elements. Evidence for enhanced abundances suggests that at least part of the thermal X-ray emission comes from ejecta.
4. The TeV gamma-ray observations allow us to determine the energy in relativistic electrons to be about 7×10^{48} erg; the current shock efficiency at accelerating electrons is about 5%, and the energy in relativistic particles is much greater than that in magnetic field.
5. We estimate that the ambient magnetic field is about $3 \mu\text{Gauss}$, and that the MHD wave spectrum near SN 1006 drops substantially in amplitude above a wavelength of about 10^{17} cm.

We have demonstrated that *sresc*, in conjunction with inhomogeneous thermal models, can describe the full remnant emission. These models (*sresc* and *srcut* in more general situations, as discussed in Section 3) represent a significant improvement over power-law models in describing the physics of synchrotron X-ray emission. We can now proceed to spatially-resolved spectral modeling of SN 1006. The true test of the escape limited synchrotron model will be its application to the spatially resolved data sets in our forthcoming paper. We will develop specialized versions of the *sresc* model to describe spatially distinct areas of SN 1006.

The National Radio Astronomy Observatory is a facility of the National Science Foundation operated under a cooperative agreement by Associated Universities, Inc. Our research made use of the

following online services: NASA’s Astrophysics Data System Abstract Service, NASA’s SkyView facility (<http://SkyView.GFSC.NASA.gov>) located at NASA Goddard Space Flight Center and SIMBAD at Centre de Données astronomiques de Strasbourg (US mirror <http://simbad.harvard.edu/Simbad>).

Thanks to J. Keohane for research notes and advice. This research is supported by NASA grant NAG5-7153 and NGT5-65 through the Graduate Student Researchers Program.

REFERENCES

- Aharonian, F. A. & Atoyan, A. M. 1999, *A&A*, 351, 330
- Allen, G. E., Keohane, J. W., Gotthelf, E. V., Petre, R., Jahoda, K., Rothschild, R. E., Lingenfelter, R. E., Heindl, W. A., Marsden, D., Gruber, D. E., Pelling, M. R., & Blanco, P. R. 1997b, *ApJ*, 487L, 97
- Allen, G. E., Petre, R., Gotthelf, E. V. & Keohane, J. 1997a, American Astronomical Society Meeting, 191, 9903
- Arnaud, K. A., 1996, *Astronomical Data Analysis Software and Systems V*, eds. Jacoby G. & Barnes J., p17, ASP Conf. Series volume 101.
- Asvarov, A. I., Guseinov, O. H., Kasumov, F. K., & Dogel', V. A. 1990, *A&A*, 229, 196
- Baring, M. G., Ellison, D. C., Reynolds, S. P., Grenier, I. A., & Goret, P. 1999, *ApJ*, 513, 311
- Becker, R. H., Szymkowiak, A. E., Boldt, E. A., Holt, S. S. & Serlemitsos, P. J. 1980, *ApJ*, 240, L33
- Berezhko, E. G., Ksenofontov, L. T., & Petukhov, S. I. 1999, *Proc. 26th Int. Cosmic-Ray Conf. (Salt Lake City)*, 4, 431
- Berezhko, E. G., Yelshin, V. K., & Ksenofontov, L. T. 1996, *Soviet Phys. JETP Lett.*, 82(1), 1
- Blair, W. P., Long, K. S. & Raymond, J. C. 1996, *ApJ*, 468, 871
- Blumenthal, G. R. & Gould, R. J. 1970, *Reviews of Modern Physics*, 42, 237
- Borkowski, K. J., Rho, J., Dyer, K. K. & Reynolds, S. P. 2000a, *ApJ*, in press
- Borkowski, K. J., Lyerly, W. J. & Reynolds, S. P. 2000b, submitted to *ApJ*
- Borkowski, K. J., Rho, J., Dyer, K. K. & Reynolds, S. P. 1999, American Astronomical Society Meeting, 195, 4313
- Dwarkadas, V. V. & Chevalier, R. A. 1998, *ApJ*, 497, 807
- Ellison, D. C., Berezhko, E. G., & Baring, M. G. 2000, *ApJ*, 540, 292
- Gaisser, T. K., Protheroe, R. J., & Stanev, T. 1998, *ApJ*, 492, 219
- Gorenstein, P. 1975, *ApJ*, 198, 95
- Green D. A. 1998, *A Catalogue of Galactic Supernova Remnants (1998 September version)*, Mullard Radio Astronomy Observatory, Cambridge, United Kingdom (available on the World-Wide-Web at "<http://www.mrao.cam.ac.uk/surveys/snrs/>").
- Grevesse, N. & Anders, E. 1989, *American Institute of Physics Conference Series*, 183, 1
- Hamilton, A. J. S., Sarazin, C. L., & Szymkowiak, A. E. 1986, *ApJ*, 300, 698
- Iwamoto, K. , Brachwitz, F. , Nomoto, K. 'I. , Kishimoto, N. , Umeda, H. , Hix, W. R. & Thielemann, F. -K. 1999, *ApJS*, 125, 439
- Jahoda, K. , Swank, J. H., Giles, A. B., Stark, M. J., Strohmayer, T. , Zhang, W. & Morgan, E. H. 1996, *Proc. SPIE*, 2808, 59

- Koyama, K., Petre, R., Gotthelf, E. V., Hwang, U., Matura, M., Ozaki, M., Holt, & S. S. 1995, *Nature* 378, 255
- Koyama, K. , Kinugasa, K. , Matsuzaki, K. , Nishiuchi, M. , Sugizaki, M. , Torii, K. , Yamauchi, S. & Aschenbach, B. 1997, *PASJ*, 49, L7
- Lagage, P. O. Cesarsky, C. J. 1983, *A&A*, 125, 249
- Laming, J. M. 1998, *ApJ*, 499, 309
- Mastichiadis, A., & de Jager, O. C. 1996, *A&A*, 311, L5
- Muraishi, H., et al. 2000, *A&A*, 354, L57
- Nomoto, K., Thielemann, F. -K., Yokoi, K. 1984 *ApJ*286, 644
- Pohl, M. 1996, *A&A*, 307, 57
- Reynolds, S. P. & Chevalier, R. A. 1981, *ApJ*, 245, 912
- Reynolds, S. P. 1996, *ApJ*, 459, L13
- Reynolds, S. P. 1997, *BullAAS*, 29, 1267
- Reynolds, S. P. 1998, *ApJ*, 493, 375
- Reynolds, S. P. 1999, *Proc. 3rd INTEGRAL Workshop: Astr.Lett.&Comm.*, 38, 425
- Reynolds, S. P. & Keohane, J. W. 1999, *ApJ*, 525, 368
- Reynolds, S. P. & Gilmore, D. M. 1986, *AJ*, 92, 1138
- Rybicki, G. B. & Lightman, A. P. 1979, *New York, Wiley-Interscience*, 1979. 393 p.,
- Slane, P. , Gaensler, B. M., Dame, T. M., Hughes, J. P., Plucinsky, P. P., & Green, A. 1999, *ApJ*, 525, 357
- Sturmer, S. J., Skibo, J. G., Dermer, C. D., & Mattox, J. R. 1997, *ApJ*, 490, 619
- Tanimori, T., et al. 1998, *ApJ*, 497, L25
- The, L. -S., Leising, M. D., Kurfess, J. D., Johnson, W. N., Hartmann, D. H., Gehrels, N., Grove, J. E. & Purcell, W. R. 1996, *A&AS*, 120, C357
- Willingale, R., West, R. G., Pye, J. P. & Stewart, G. C. 1996, *MNRAS*, 278, 749
- Vink, J. , Kaastra, J. S. & Bleeker, J. A. M. 1997, *A&A*, 328, 628
- Vink, J., Kaastra, J. S., Bleeker, J. A. M. & Preite-Martinez, A. 2000, *A&A*, 354, 931

Table 1. *RXTE* Observations of SN 1006 AD

Parameter	<i>RXTE</i> PCA
Cycle	A01 Epoch 1
Date	1996 Feb 18-19
Pointing center α	$15^h 04^m 00^s.00$
β (J2000)	$-41^\circ 48' 00''.0$
Exposure (ks)	6.6
Counts (k)	477
Effective Resolution	1° FWHM
Field of view	1°
Energy range	2-60 keV

Table 2. Select *ASCA* observations of SN 1006 AD

Parameter	Center	Northeast	Southwest
Cycle	PV	PV	AO4
Date	1993 Aug 19	1993 September 13	1996 February 20
Pointing center α	$15^h 02^m 48^s.24$	$15^h 03^m 31^s.92$	$15^h 02^m 34^s.32$
β (J2000)	$-41^\circ 55' 45''.8$	$-41^\circ 46' 25''.0$	$-42^\circ 02' 57''.8$
Exposure (ks)	23	23	22

Table 3. Datasets Fit For This Paper

Parameter	North Limb		Full Remnant	
	ASCA SIS	ASCA GIS	ASCA GIS	RXTE PCA
Date	1993 September 13	1993 September 13	1993-1996	1996 Feb 18-19
Average Pointing center α	$15^h 03^m 55^s$	$15^h 03^m 55^s$	$15^h 02^m 58^s$	$15^h 04^m 00^s$
β (J2000)	$-41^\circ 46' 00''$	$-41^\circ 46' 00''$	$-41^\circ 33' 02''$	$-41^\circ 48' 00''$
Total Exposure (ks)	104	104	136	6.6
Total Counts (k)	33	14	258	477
Background from	chip	night sky	night sky	model
Background Counts (k)	4	144	9400	5.46 (from model)
Spatial area used	$\sim 10'$	$\sim 10'$	$\sim 78' \times 103'$	$\sim 2^\circ$
Energy range	0.6-10.0 keV	0.6-10.0 keV	0.6-10.0 keV	3.0-10.0 keV

Table 4. Model Fits to ASCA GIS & RXTE PCA observations of SN 1006 AD

Parameters	<i>nei</i>	<i>vpshock</i>	<i>vpshock</i> + power-law	<i>vpshock</i> + <i>sresc</i>
χ^2/DOF	7463/2285	3237/2279	2721/2279	2709/2280
χ^2_ν	3.27	1.42	1.19	1.19
PCA / GIS	0.70	0.63	0.64	0.64
kT [keV]	1.63 ^{1.62} _{1.64}	2.18 ^{2.13} _{2.22}	1.79 ^{1.84} _{1.74}	0.60 ^{0.70} _{0.52}
τ [s cm ⁻³]	7.3E8 ^{7.42} _{7.18}	3.3E9 ^{3.07} _{3.35}	2.9E9 ^{3.14} _{2.72}	3.8E9 ^{***} _{3.6}
Abundances:				
O	1	8.2E-2 ^{9.3E-2} _{7.0E-2}	8.6E-2 ^{9.9E-1} _{7.4E-2}	3.2E-2 ^{3.7E-2} _{2.0E-2}
Ne	1	2.8E-1 ^{3.1E-1} _{2.5E-1}	2.5E-1 ^{2.9E-1} _{2.2E-1}	1.0E-1 ^{1.2E-1} _{6.8E-2}
Mg	1	1.5E0 ^{1.6E0} _{1.4E0}	1.2E0 ^{1.4E0} _{1.1E0}	4.4E-1 ^{5.2E-1} _{3.0E-1}
Si	1	1.0E0 ^{1.1E0} _{9.3E-1}	1.0E0 ^{1.1E0} _{9.2E-1}	1.0E0 ^{***} _{6.9E-1}
S	1	5.3E-1 ^{6.6E-1} _{4.2E-1}	7.4E-1 ^{9.3E-1} _{5.8E-1}	2.2E0 ^{2.5E0} _{1.5E0}
Fe	1	1.9E0 ^{2.4E0} _{1.6E0}	2.5E0 ^{3.3E0} _{1.8E0}	2.1E0 ^{2.8E0} _{1.4E0}
Normalization ¹	0.24 ^{0.25} _{0.23}	0.15 ^{0.16} _{0.14}	0.11 ^{0.111} _{0.105} /2E-2	0.61 ^{0.63} _{0.58} /19.0
Nonthermal	$\Gamma=2.50$ ^{2.63} _{2.34} keV ₋₁ cm ₋₂ s ₋₁	<i>rolloff</i> =3.0E17 ^{3.1} _{2.8} Hz
Flux [ergs cm ⁻² s ⁻¹]	2.0E-10	1.9E-10	1.3E-10/5.6E-11	5.0E-11/1.3E-10

***In some cases it was not possible to establish errors on certain values. See Section 4 for discussion.

¹Normalization represents different physical quantities: For thermal models *norm* is the emission measure. For a powerlaw *norm* is flux at 1 keV in photons keV⁻¹ cm⁻² s⁻¹. For *sresc norm* is the 1 GHz radio flux.

Table 5. Mass of Elements in SN 1006

Element, [M _⊙]	<i>vpshock</i>	W7	Core Collapse
O	3.5E-2 ^{3.9E-2} _{2.7E-2}	1.4E-1	1.8E0
Ne	2.0E-2 ^{2.3E-2} _{1.8E-2}	4.5E-3	2.3E-1
Mg	3.3E-2 ^{3.7E-2} _{3.0E-2}	8.6E-3	1.2E-1
Si	8.1E-2 ^{1.6E-1} _{7.3E-2}	1.6E-1	1.2E-1
S	9.5E-2 ^{1.2E-1} _{7.7E-2}	8.7E-2	4.1E-2
Fe	4.5E-1 ^{5.0E-1} _{3.9E-1}	7.5E-1	9.1E-2

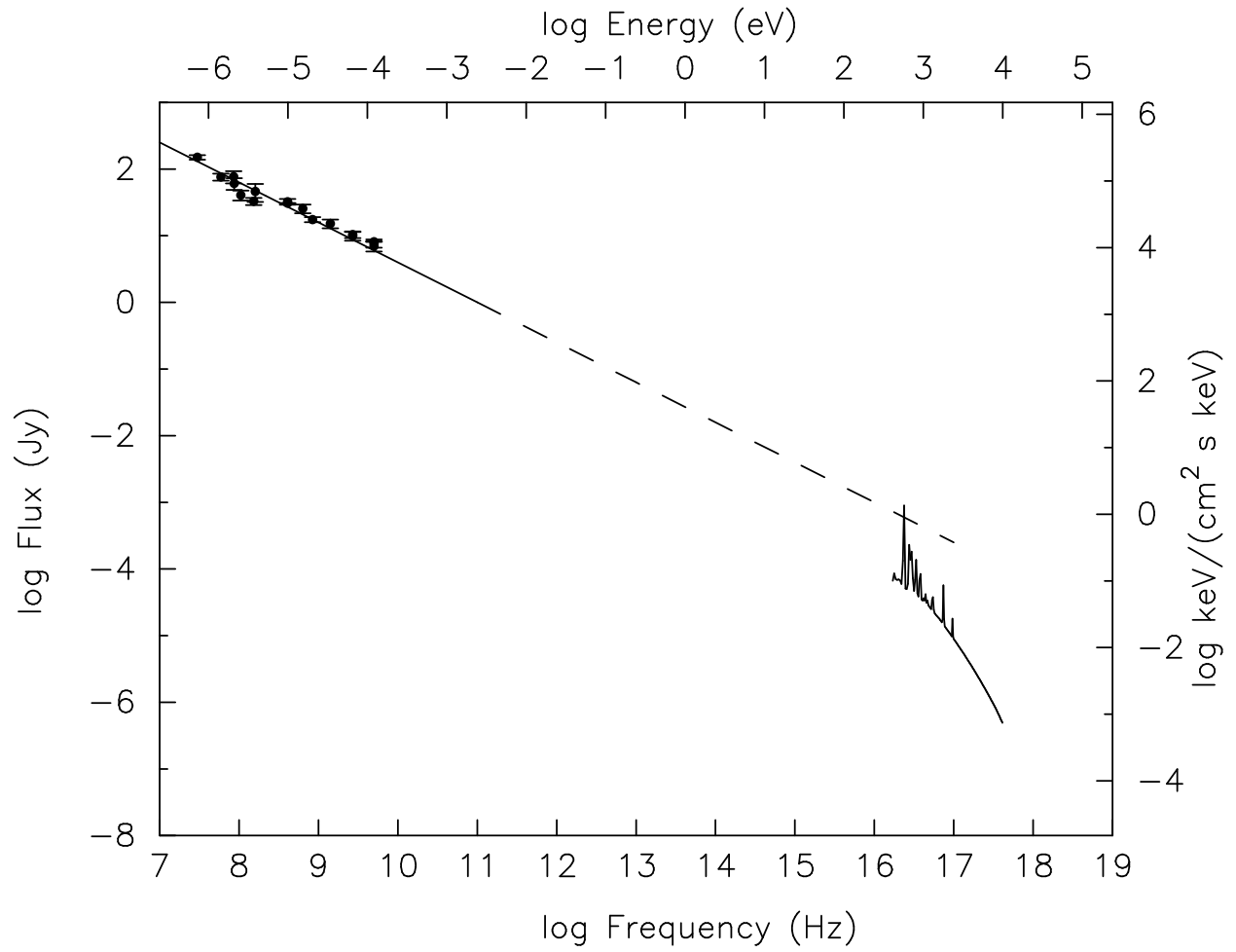


Fig. 1.— The radio flux measurement with a power law spectrum extrapolated to X-ray energies. The X-rays are the unfolded ASCA spectrum, shown only for comparison.

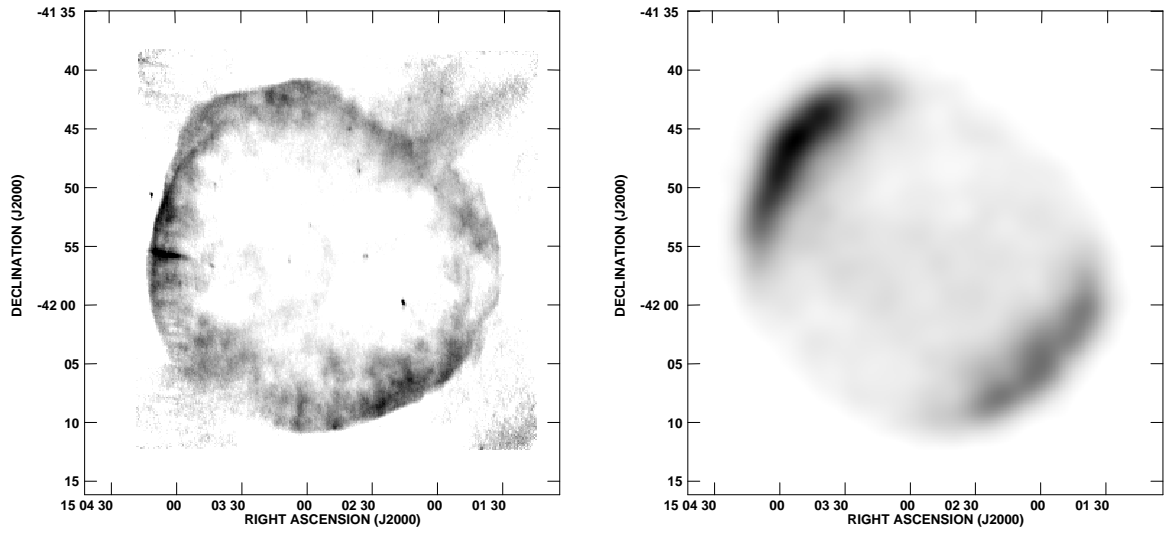


Fig. 2.— a) VLA image of SN 1006 AD resolution $12'' \times 7''$, corrected for the primary beam. b) ASCA GIS 3 convolved to $60''$

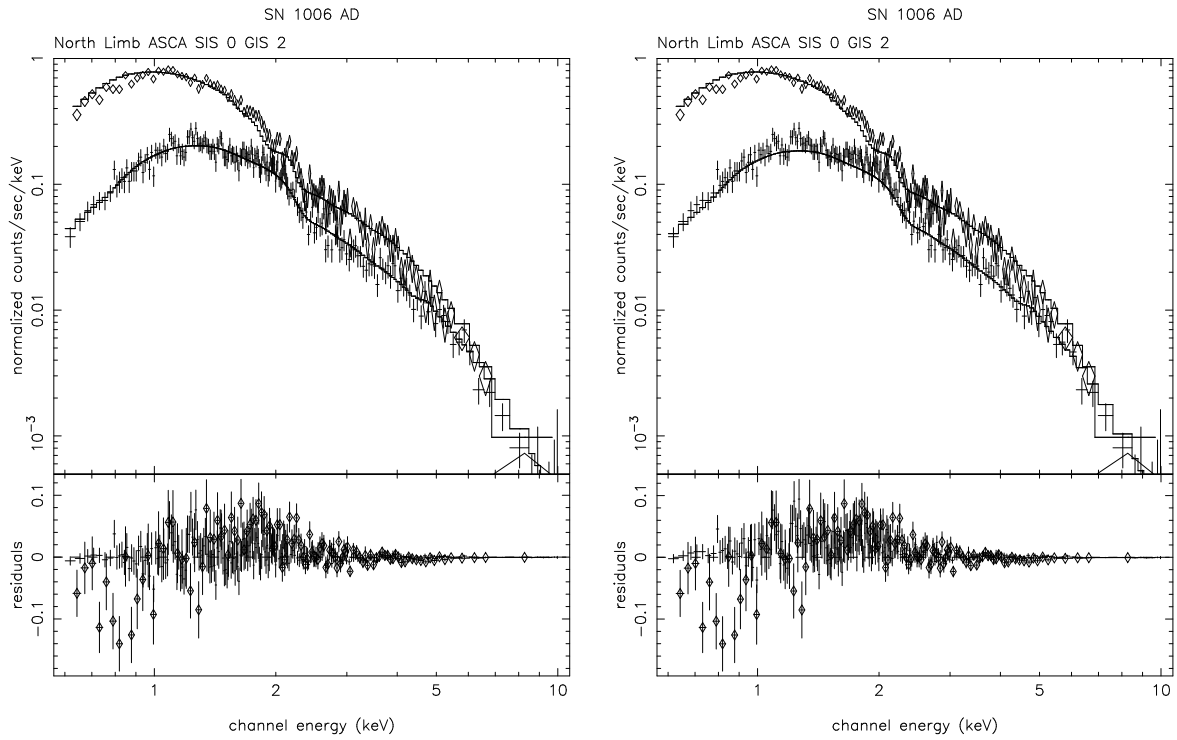


Fig. 3.— ASCA SIS 0 & 1 GIS 2 & 3 (only SIS 0 (crosses) and GIS 2 (diamonds) are shown) taken from the north rim, fit by a) power-law and b) *sresc*. Parameters for the fits are given in §4.1.

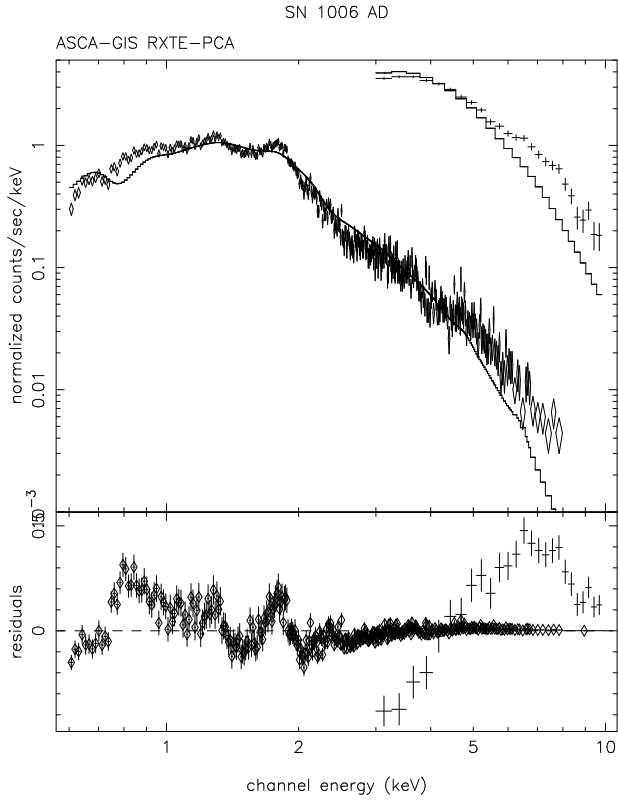


Fig. 4.— The *nei* model fit to the full remnant ASCA GIS (diamonds) and *RXTE* PCA (crosses). Parameters listed in Table 3, column 2.

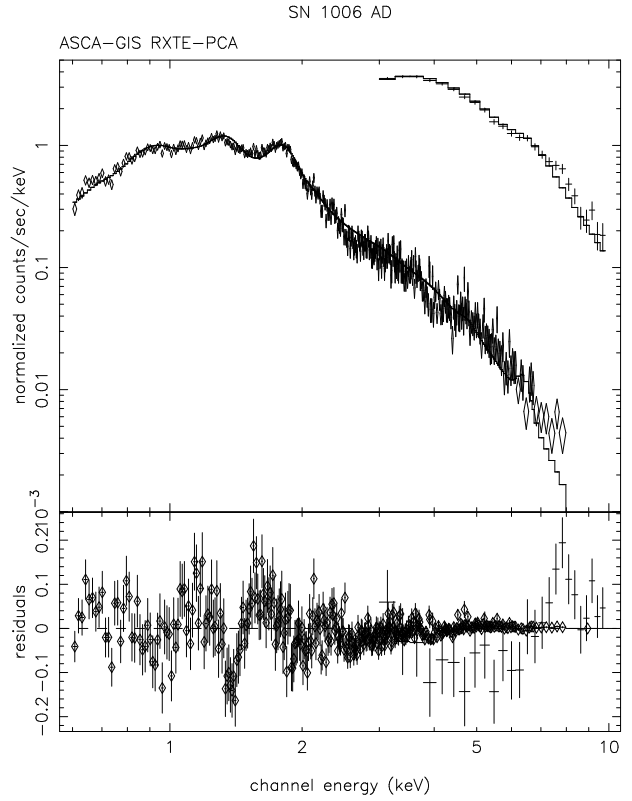


Fig. 5.— The *vps shock* model applied to the full remnant ASCA GIS (diamonds) and *RXTE* PCA (crosses). Parameters listed in Table 3, column 3.

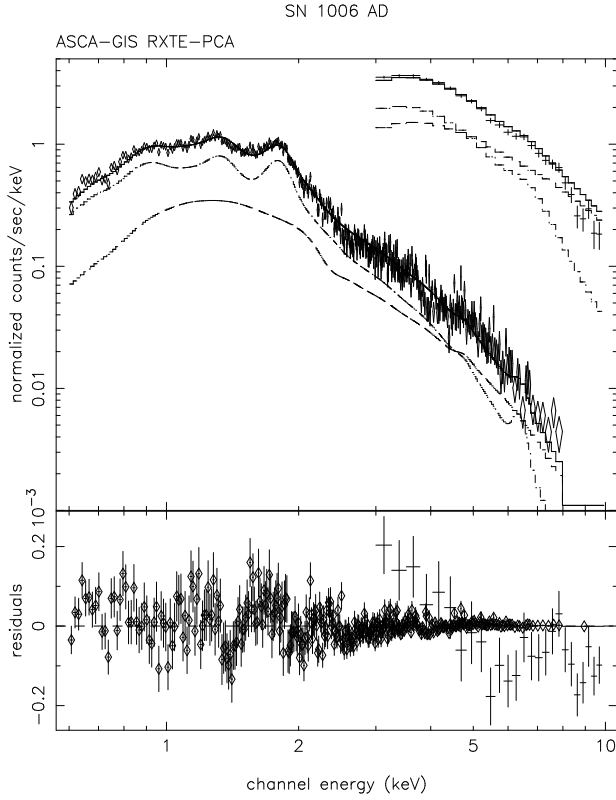


Fig. 6.— The *vpshock* + power-law model applied to the full remnant *ASCA* GIS (diamonds) and *RXTE* PCA (crosses). The solid line is the total model while the broken lines represent the individual contributions: the smooth varying broken line is power-law while the *vpshock* shows prominent spectral lines. Parameters listed in Table 3, column 4.

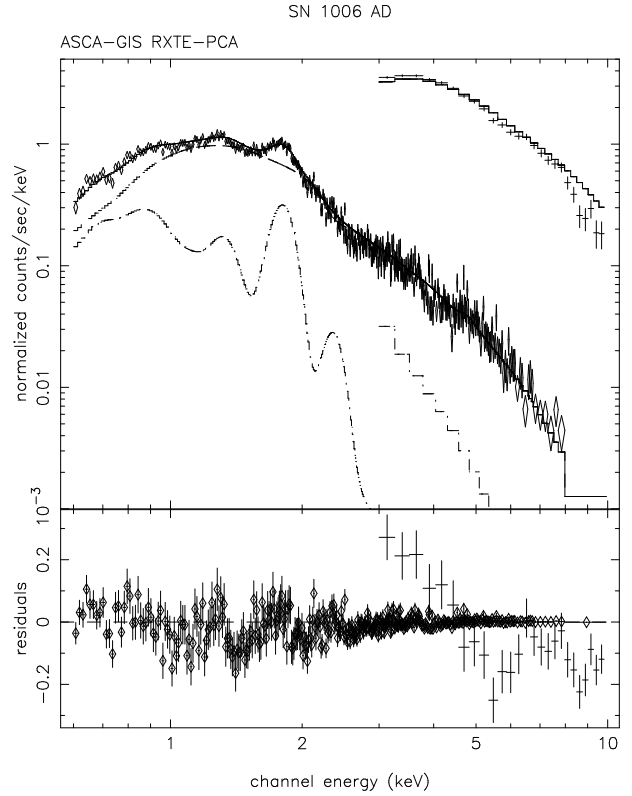


Fig. 7.— The *vpshock* + *sresc* model fit to whole remnant *ASCA* GIS (diamonds) and *RXTE* PCA (crosses). The solid line is the total model while the broken lines represent the individual contributions: the smooth varying broken line is *sresc* while the *vpshock* shows prominent spectral lines. Parameters listed in Table 3, column 5.

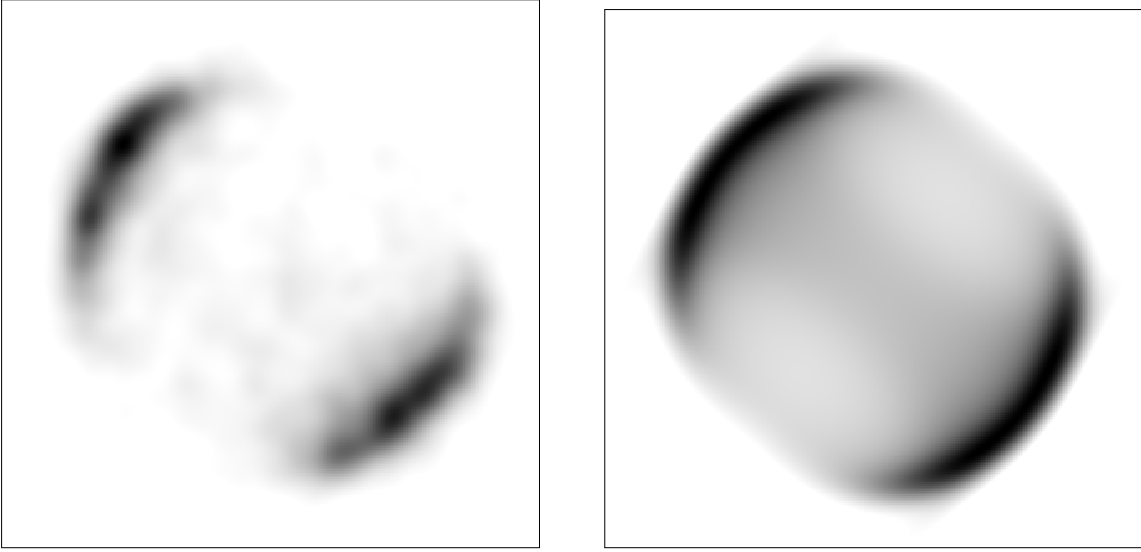


Fig. 8.— a) GIS image from 2-10 keV, energies dominated by synchrotron. b) The synchrotron X-ray image predicted by the *sresc* model fitted parameters $rolloff=3.0\times 10^{17}$, $\alpha=0.6$, $norm(1\text{ GHz flux})=19\text{ Jy}$. We have assumed a uniform upstream magnetic field of $3\ \mu\text{G}$ and a compression ratio of 4. Both images are convolved to $2'$

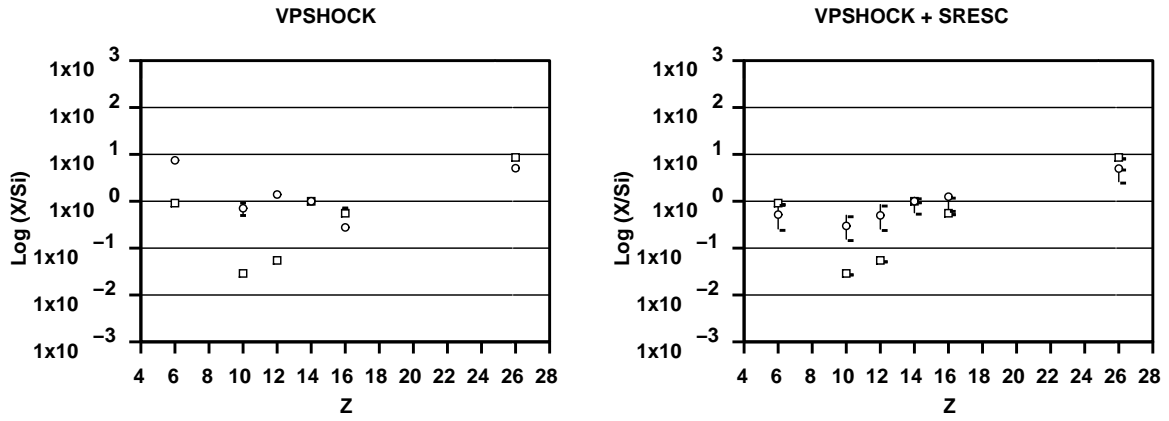


Fig. 9.— Abundances measured by a) *vpshock* model (circles) and b) *vpshock* + *sresc* (circles) compared to the W7 supernova model from Iwamoto et al. (1999) (squares), normalized to silicon (by mass).

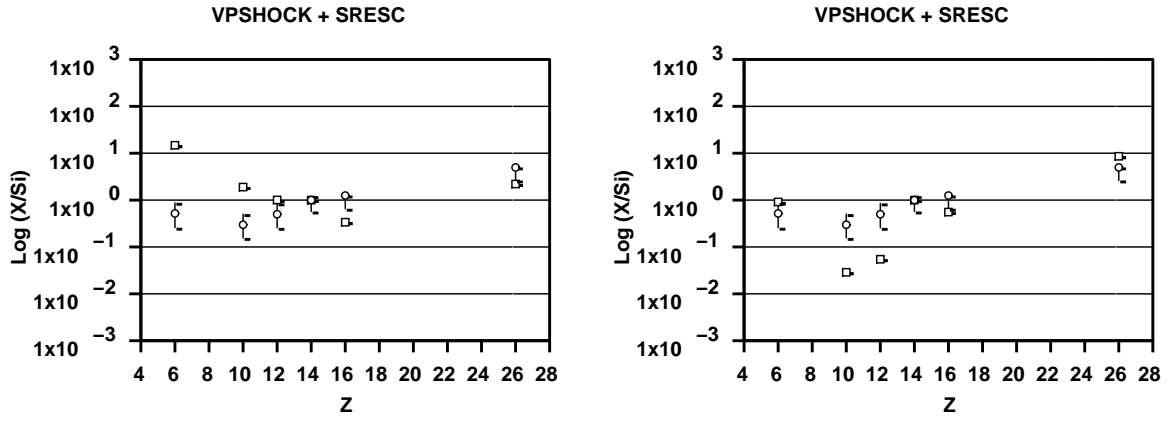


Fig. 10.— Abundances measured by *vpshock* + *sresc* (circles) compared to a) Type II SNR b) Type Ia (W7) SNR predictions from Iwamoto et al. (1999) (squares), normalized to silicon (by mass).

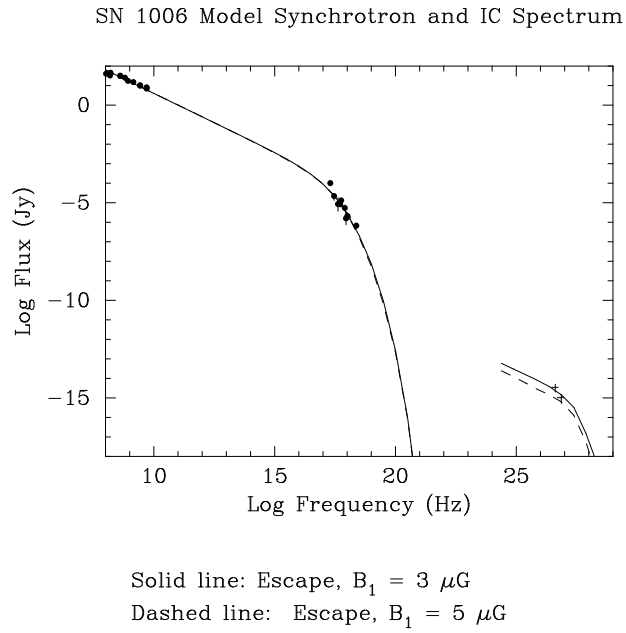


Fig. 11.— Two gamma-ray spectra, for $B_1 = 3$ and $5 \mu\text{gauss}$ ($r = 4$), constrained to have the same value of $norm$, i.e., varying in K .

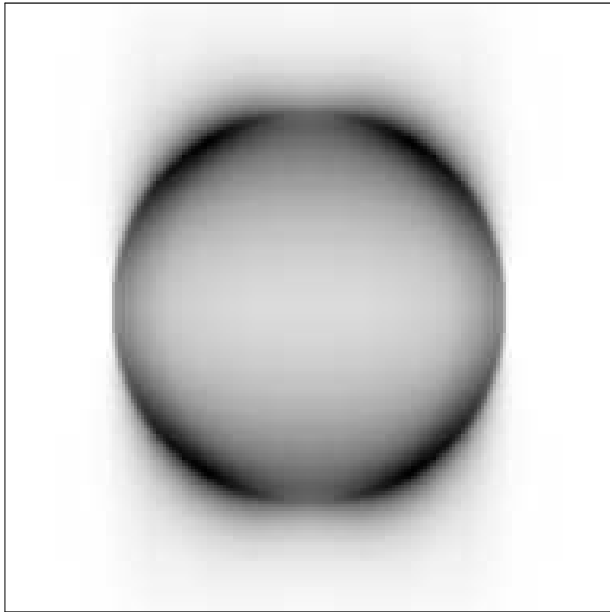


Fig. 12.— The predicted image of gamma-ray emission at an energy of 1 TeV.